









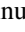










The NANOGrav 11 yr Data Set: Solar Wind Sounding through Pulsar Timing

D. R. Madison^{1,2,3} , J. M. Cordes^{4,5} , Z. Arzoumanian⁶, S. Chatterjee^{4,5} , K. Crowter⁷, M. E. DeCesar⁸ , P. B. Demorest⁹,
T. Dolch¹⁰ , J. A. Ellis^{2,3}, R. D. Ferdman¹¹, E. C. Ferrara¹², E. Fonseca¹³, P. A. Gentile^{2,3}, G. Jones¹⁴, M. L. Jones^{2,3},
M. T. Lam^{2,3} , L. Levin^{2,3} , D. R. Lorimer^{2,3}, R. S. Lynch¹⁵ , M. A. McLaughlin^{2,3} , C. M. F. Mingarelli¹⁶, C. Ng^{7,17},
D. J. Nice⁸ , T. T. Pennucci¹⁸ , S. M. Ransom¹ , P. S. Ray¹⁹ , R. Spiewak^{20,21} , I. H. Stairs⁷ , K. Stovall⁹ ,
J. K. Swiggum²¹ , and W. W. Zhu^{22,23}

¹ The National Radio Astronomy Observatory, 520 Edgemont Rd., Charlottesville, VA, 22903, USA; dmadison@nrao.edu

² Department of Physics and Astronomy, West Virginia University, P.O. Box 6315, Morgantown, WV 26506, USA

³ Center for Gravitational Waves and Cosmology, West Virginia University, Chestnut Ridge Research Building, Morgantown, WV 26505, USA

⁴ Department of Astronomy, Cornell University, 616-A Space Sciences Building, Ithaca, NY 14853, USA

⁵ Cornell Center for Astrophysics and Planetary Science, 104 Space Sciences Building, Ithaca, NY 14853, USA

⁶ Center for Research and Exploration in Space Science and Technology and X-Ray Astrophysics Laboratory, NASA Goddard Space Flight Center, Code 662, Greenbelt, MD 20771, USA

⁷ Department of Physics and Astronomy, University of British Columbia, 6224 Agricultural Rd., Vancouver, BC V6T 1Z1, Canada

⁸ Department of Physics, Lafayette College, Easton, PA 18042, USA

⁹ The National Radio Astronomy Observatory, 1003 Lopezville Rd., Socorro, NM 87801, USA

¹⁰ Department of Physics, Hillsdale College, 33 E. College St., Hillsdale, MI 49242, USA

¹¹ School of Chemistry, University of East Anglia, Norwich, NR4 7TJ, UK

¹² NASA Goddard Space Flight Center, Greenbelt, MD 20771, USA

¹³ Department of Physics, McGill University, 3600 University St., Montreal, QC H3A 2T8, Canada

¹⁴ Department of Physics, Columbia University, New York, NY 10027, USA

¹⁵ Green Bank Observatory, P.O. Box 2, Green Bank, WV 24944, USA

¹⁶ Center for Computational Astrophysics, Flatiron Institute, 162 5th Ave., New York, NY 10010, USA

¹⁷ Dunlap Institute for Astronomy and Astrophysics, University of Toronto, 50 St. George St., Toronto, ON M5S 3H4, Canada

¹⁸ Institute of Physics, Eötvös Loránd University, Pázmány P.s. 1/A, 1117 Budapest, Hungary

¹⁹ Space Science Division, Naval Research Laboratory, Washington, DC 20375-5352, USA

²⁰ Centre for Astrophysics and Supercomputing, Swinburne University of Technology, P.O. Box 218, Hawthorn, Victoria 3122, Australia

²¹ Center for Gravitation, Cosmology and Astrophysics, Department of Physics, University of Wisconsin-Milwaukee, P.O. Box 413, Milwaukee, WI 53201, USA

²² National Astronomical Observatories, Chinese Academy of Science, 20A Datun Rd., Chaoyang District, Beijing 100012, People's Republic of China

²³ Max Planck Institute for Radio Astronomy, Auf dem Hügel 69, D-53121 Bonn, Germany

Received 2018 August 16; revised 2019 January 24; accepted 2019 January 24; published 2019 February 20

Abstract

The North American Nanohertz Observatory for Gravitational Waves (NANOGrav) has observed dozens of millisecond pulsars for over a decade. We have accrued a large collection of dispersion measure (DM) measurements sensitive to the total electron content between Earth and the pulsars at each observation. All lines of sight cross through the solar wind (SW), which produces correlated DM fluctuations in all pulsars. We develop and apply techniques for extracting the imprint of the SW from the full collection of DM measurements in the recently released NANOGrav 11 yr data set. We filter out long-timescale DM fluctuations attributable to structure in the interstellar medium and carry out a simultaneous analysis of all pulsars in our sample that can differentiate the correlated signature of the wind from signals unique to individual lines of sight. When treating the SW as spherically symmetric and constant in time, we find the electron number density at 1 au to be $7.9 \pm 0.2 \text{ cm}^{-3}$. We find our data to be insensitive to long-term variation in the density of the wind. We argue that our techniques paired with a high-cadence, low-radio-frequency observing campaign of near-ecliptic pulsars would be capable of mapping out large-scale latitudinal structure in the wind.

Key words: ISM: structure – pulsars: general – solar wind

1. Introduction

The North American Nanohertz Observatory for Gravitational Waves (NANOGrav) has entered a second decade of precisely timing an array of millisecond pulsars in an effort to detect extremely low-frequency (\sim nHz) gravitational waves (Arzoumanian et al. 2018a, 2018b). As part of this effort, NANOGrav has conducted a careful accounting of the noise processes influencing our measurements, with particular attention paid to the effects of the interstellar medium (ISM; Lam et al. 2015, 2016, 2017; Levin et al. 2016; Jones et al. 2017; Wang & Han 2018). The Parkes Pulsar Timing Array and European Pulsar Timing Array, other major efforts to detect nanohertz gravitational waves through pulsar timing, also make considerable efforts to understand and mitigate the

influence of the ISM in their timing observations (e.g., Keith et al. 2013; Caballero et al. 2016).

Pulse times of arrival (TOA) are primarily influenced by the ISM through variable dispersive delays. At a radio frequency ν , the light propagating from a pulsar to the Earth is delayed by an amount $t_d = \mathcal{D}(t)/(K\nu^2)$, where

$$\mathcal{D}(t) = \int_{\hat{n}(t)} n_e(t, \mathbf{r}) dl \quad (1)$$

is the dispersion measure (DM), typically expressed in pc cm^{-3} , $K = 2.41 \times 10^{-4} \text{ MHz}^{-2} \text{ pc cm}^{-3} \text{ s}^{-1}$, and $n_e(t, \mathbf{r})$ is the electron number density at time t and position \mathbf{r} . The integration path extends from the Earth to the pulsar along the

direction $\hat{n}(t)$, the unit vector pointing toward the pulsar from Earth at time t .

The solar wind (SW), streams of electrons flowing outward from the Sun (Parker 1958; Schwenn 2006), has a distinct and sizable influence on the DM of many pulsars. Over the course of a year, the line of sight (LOS) to a pulsar will sweep out an elliptical cone through the SW, causing annual fluctuations in DM that peak when the Sun and pulsar are in conjunction. The fluctuations are larger and more peaked for pulsars closer to the ecliptic as the LOS for these pulsars more closely approaches the Sun.

Shortly after they were discovered, pulsars were recognized as useful probes of the SW and corona (Counselman & Shapiro 1968; Hollweg 1968). The Crab Pulsar, with an ecliptic latitude $\beta = -1^\circ.24$, has been observed extensively for such applications (Goldstein & Meisel 1969; Counselman & Rankin 1972). TEMPO and TEMPO2 (Edwards et al. 2006; Nice et al. 2015), software packages commonly used for pulsar timing, both include constant, spherically symmetric models for the SW that attempt to account for timing perturbations it causes. Arzoumanian et al. (2018b) recently demonstrated that NANOGrav’s sensitivity to gravitational waves has progressed to the point that our upper limit on the amplitude of the gravitational wave stochastic background depends on our choice of solar system ephemeris. To combat this undesirable model dependence, they developed tools for bridging various ephemerides, allowing the pulsar timing data itself to inform the ephemeris.

A need has arisen for a similar treatment of the SW in which pulsar timing data can be used to inform models of the SW. As evidence for this need, Archibald et al. (2018) recently published important new constraints on general relativity’s strong equivalence principle based on observations of a pulsar in a hierarchical triple system. They explicitly discuss issues they faced when trying to include data collected while the pulsar was close to the Sun and maximally influenced by the SW. Building on techniques used by, for example, Splaver et al. (2005) and Lommen et al. (2006), Archibald et al. (2018) adapted the parameters of the SW to their data, but these techniques proved insufficient, and systematic artifacts were left behind in their data. With observations of a lone pulsar, it is not possible to fully disentangle the influence of the ISM from that of the SW, and it is difficult to constrain spatial and temporal variations in the SW. These purposes are better served by an analysis of data from a large array of pulsars, and in this work, we develop and use the techniques necessary to do just that.

In nautical parlance, to “sound” is to measure the depth of a body of water, often in fathoms. One common sounding technique is to measure the time it takes for pulses of sound to travel from a ship, bounce off the sea floor, and return to the ship. This is not altogether dissimilar from the techniques we develop in this work: pulsed radio waves, delayed by propagation through a medium of interest—the SW—are used to probe the distribution of that medium.

In Section 2, we describe the data we use for our analysis. In Section 3, we describe DM fluctuations caused by the SW and the ISM and the models for those fluctuations we apply to our data. In Section 4, we lay out the procedure by which we apply our DM fluctuation model to the data. In Section 5, we summarize and discuss the results of our modeling effort.

Finally, in Section 6 we discuss future prospects for investigations such as this and offer some concluding remarks.

2. Data

To correct delays in TOAs caused by variations in DM, NANOGrav conducts at least two observations in widely separated radio frequency bands for every observing epoch of every pulsar in our array. For data collected with the 305 m William E. Gordon Telescope of the Arecibo Observatory, observations are normally taken using two separate receivers on the same day; depending on the pulsar, these are either the 430 MHz and 1.4 GHz receivers or the 1.4 GHz and 2.3 GHz receivers (or, in one case, the 327, 430, and 1400 MHz receivers). For data collected with the 100 m Robert C. Byrd Green Bank Telescope (GBT), observations are typically taken at 800 MHz and 1.4 GHz, usually within the same week (for exact center frequencies and bandwidths, see Table 1 of The NANOGrav Collaboration et al. 2015). While using non-simultaneous timing observations to infer DM can induce measurement biases because the true DM varies by some amount between the measurements (Lam et al. 2015; Niu et al. 2017), these errors are typically small—Jones et al. (2017) showed that most DM variation timescales are greater than the observation cadence—and we ignore them. Furthermore, Cordes et al. (2016) recently expounded on how scattering causes light from multiple paths to converge on the observer, making the observed DM an effective average over many paths. Since scattering varies with radio frequency, so too will DM. We acknowledge but ignore this phenomenon in this work as it is particularly important at radio frequencies lower than those we deal with. For detailed information regarding the center frequencies and bandwidths of our observations, see Table 1. All data are available online²⁴ and described in more detail in Arzoumanian et al. (2018a).

A nominal DM, \mathcal{D}_0 , and a time series of perturbations to the nominal DM, $\delta\mathcal{D}(t_i)$ (where t_i is the centroid of a bin of multifrequency TOAs), are included as free parameters in a pulsar timing model and constrained by the TOAs using generalized least-squares fitting techniques common in the practice of pulsar timing (Edwards et al. 2006; van Haasteren & Levin 2013; Vigeland & Vallisneri 2014). It is these time series of DM fluctuations, $\delta\mathcal{D}(t_i)$, that we use as a starting point for our analysis. The linearized timing model \mathbf{M} , paired with a noise model \mathbf{C} , yields a parameter covariance matrix $\mathbf{C}_p = (\mathbf{M}^T \mathbf{C}^{-1} \mathbf{M})^{-1}$. A subblock of \mathbf{C}_p that is symmetric about the diagonal describes covariances in the measured time series $\delta\mathcal{D}(t_i)$; we call this subblock $\mathbf{\Sigma}$ and its i th diagonal element σ_i^2 . Since the time series $\delta\mathcal{D}(t_i)$ is defined as variation about \mathcal{D}_0 , it is constrained to have a zero weighted mean. As such, $\mathbf{\Sigma}$ has a null eigenvalue and is not invertible. We define $\mathbf{\Xi} = \mathbf{E}^T \mathbf{F} \mathbf{E}$, where \mathbf{F} is a diagonal matrix containing the nonzero eigenvalues of $\mathbf{\Sigma}$ and the columns of \mathbf{E} are the associated eigenvectors. Then $\mathbf{\Xi}$ is invertible: $\mathbf{\Xi}^{-1} = \mathbf{E}^T \mathbf{F}^{-1} \mathbf{E}$.

A small number of NANOGrav observations were pared from the 11 yr data release after being deemed too influenced by the SW (Arzoumanian et al. 2018a). If the anticipated SW-induced time delay between observations at different bands exceeded 160 ns, the data were excluded or separated into different observing epochs. Anticipated delays were inferred from a spherically symmetric model of the SW with a purely inverse square radial

²⁴ data.nanograv.org

Table 1
Amplitude and Phase of Annual Sinusoidal DM Fluctuations from the ISM

PSR	$\hat{a} \times 10^5$ (pc cm ⁻³)	$\hat{b} \times 10^5$ (pc cm ⁻³)	$\hat{A} \times 10^5$ (pc cm ⁻³)	$\hat{\Phi}$ (deg)
J0023+0923	21.2 ± 7.2	-9.1 ± 6.3	23.1 ± 7.2	113.1 ± 16.0
J0030+0451	-5.2 ± 3.4	-1.7 ± 3.8	5.5 ± 3.7	-108.1 ± 37.2
J0340+4130	6.4 ± 5.0	-12.7 ± 6.0	14.3 ± 5.5	153.0 ± 22.3
J0613-0200	2.3 ± 1.6	10.6 ± 1.7	10.9 ± 1.7	12.6 ± 8.4
J0636+5128	-6.1 ± 4.0	12.7 ± 5.7	14.1 ± 5.3	-25.9 ± 18.1
J0645+5158	6.4 ± 3.4	2.5 ± 2.4	6.8 ± 3.1	68.4 ± 23.2
J0740+6620	0.0 ± 10.0	-9.6 ± 11.1	9.6 ± 11.1	179.9 ± 59.5
J0931-1902	6.1 ± 8.7	-30.7 ± 8.3	31.3 ± 8.3	168.6 ± 16.1
J1012+5307	6.6 ± 2.8	2.8 ± 3.8	7.2 ± 3.3	67.1 ± 27.0
J1024-0719	5.6 ± 3.6	0.4 ± 2.4	5.6 ± 3.5	85.6 ± 26.4
J1125+7819	158.8 ± 96.4	-91.3 ± 92.8	183.1 ± 84.6	119.8 ± 32.4
J1453+1902	-13.7 ± 18.1	24.3 ± 22.4	27.9 ± 22.5	-29.3 ± 36.6
J1455-3330	16.7 ± 9.1	-6.2 ± 9.0	17.8 ± 9.2	110.3 ± 28.5
J1600-3053	-5.0 ± 2.7	0.3 ± 2.8	5.0 ± 2.7	-85.8 ± 32.8
J1614-2230	-3.6 ± 2.8	11.2 ± 2.6	11.8 ± 2.7	-17.9 ± 13.4
J1640+2224	-3.5 ± 1.0	-3.7 ± 1.1	5.1 ± 1.2	-136.2 ± 11.5
J1643-1224	-29.0 ± 11.4	28.5 ± 11.9	40.7 ± 11.0	-45.4 ± 17.2
J1713+0747	-1.5 ± 0.6	0.3 ± 0.7	1.6 ± 0.7	-78.7 ± 26.0
J1738+0333	-28.4 ± 13.0	22.4 ± 11.3	36.2 ± 12.1	-51.7 ± 19.4
J1741+1351	3.7 ± 3.4	9.3 ± 3.1	10.1 ± 3.7	22.0 ± 16.3
J1744-1134	-3.9 ± 2.7	-1.5 ± 2.9	4.2 ± 2.8	-111.2 ± 38.5
J1747-4036	29.4 ± 39.1	68.1 ± 35.1	74.2 ± 36.2	23.3 ± 29.4
J1832-0836	-7.6 ± 6.8	-44.3 ± 6.2	45.0 ± 6.3	-170.2 ± 8.5
J1853+1303	36.8 ± 28.6	-1.2 ± 23.2	36.8 ± 28.8	91.9 ± 35.9
B1855+09	-2.6 ± 2.2	1.8 ± 2.2	3.2 ± 2.2	-54.7 ± 41.3
J1903+0327	-110.3 ± 27.5	60.3 ± 32.7	125.7 ± 25.1	-61.3 ± 15.7
J1909-3744	-3.3 ± 0.7	5.9 ± 0.9	6.8 ± 0.9	-29.4 ± 6.8
J1910+1256	-1.4 ± 11.1	28.8 ± 9.6	28.8 ± 9.6	-2.9 ± 22.0
J1911+1347	-11.3 ± 2.5	16.5 ± 2.1	20.0 ± 2.3	-34.4 ± 6.7
J1918-0642	-0.2 ± 1.9	7.0 ± 2.2	7.0 ± 2.1	-2.2 ± 15.5
J1923+2515	-2.2 ± 5.2	-12.3 ± 4.8	12.5 ± 5.2	-169.7 ± 21.9
B1937+21	-20.5 ± 4.7	13.9 ± 4.7	24.8 ± 4.6	-55.8 ± 11.2
J1944+0907	-7.3 ± 6.6	26.5 ± 7.1	27.5 ± 6.4	-15.4 ± 15.1
B1953+29	-2.4 ± 19.5	21.9 ± 20.1	22.1 ± 19.2	-6.4 ± 53.1
J2010-1323	-2.7 ± 2.5	1.8 ± 2.9	3.2 ± 2.4	-55.5 ± 52.1
J2017+0603	-0.2 ± 5.0	-41.4 ± 6.3	41.4 ± 6.3	-179.6 ± 6.9
J2033+1734	8.1 ± 13.6	21.4 ± 17.9	22.9 ± 19.0	20.7 ± 30.3
J2043+1711	2.2 ± 3.6	-8.3 ± 3.1	8.6 ± 3.1	165.1 ± 24.2
J2145-0750	1.0 ± 8.0	5.7 ± 7.5	5.8 ± 7.6	9.9 ± 77.8
J2214+3000	-81.7 ± 29.2	62.6 ± 27.7	102.9 ± 28.9	-52.5 ± 15.6
J2229+2643	-2.8 ± 3.5	3.8 ± 4.1	4.7 ± 3.7	-36.7 ± 48.6
J2234+0611	-6.6 ± 4.8	-2.7 ± 6.0	7.1 ± 5.6	-112.4 ± 42.2
J2234+0944	13.0 ± 19.8	62.2 ± 21.8	63.5 ± 20.6	11.8 ± 18.9
J2302+4442	9.2 ± 16.3	19.5 ± 14.1	21.5 ± 15.0	25.2 ± 41.4
J2317+1439	0.9 ± 2.0	8.0 ± 2.3	8.1 ± 2.3	6.9 ± 14.1

Note. Best-fit amplitude and 1σ uncertainty on the amplitudes, \hat{a} and \hat{b} , of sinusoidal annual fluctuations in DM associated with the ISM. The quantities \hat{A} and $\hat{\Phi}$ are functions of \hat{a} and \hat{b} as described in the text preceding Equation (16).

density profile and a fixed electron density at 1 au of 5 cm^{-3} . The motivation for this practice is that insufficient mitigation of the timing perturbations from the SW when pulsars appear very near the Sun could deleteriously influence NANOGrav's various gravitational wave investigations. While the few observations for which the SW is most influential have been removed from the data release, we will see that it is still clearly important for describing our DM time series.

3. Physical Model of Dispersion Measure Fluctuations

We treat the DM time series for a pulsar, $\mathcal{D}(t_i) = \mathcal{D}_0 + \delta\mathcal{D}(t_i)$, as a sum of two terms: contributions from the ISM, $\mathcal{I}(t_i)$,

and contributions from the SW, $\mathcal{W}(t_i)$. We now discuss each of these contributions in detail, specifically how we model them.

3.1. The SW

The number density of electrons in the SW can be modeled as

$$n_{\odot}(t, r, \lambda, \beta) = \sqrt{4\pi} \sum_{l,m} n_{lm}(t) Y_{lm}(\lambda, \beta) \left(\frac{1 \text{ au}}{r} \right)^2, \quad (2)$$

where n_{lm} is a coefficient for the real spherical harmonic Y_{lm} . The coordinates λ and β are ecliptic longitude and latitude,

respectively. This is a completely general form for a time-dependent field with an inverse square radial profile. An inverse square radial density profile follows from a wind ejected radially outward at a fixed velocity. Issautier et al. (1998), using in situ measurements from the *Ulysses* space probe, found this inverse square scaling to hold almost exactly in far southern ecliptic latitudes. For northern latitudes, they find a steeper radial scaling for the electron density: $n_e \propto r^{-2.36}$ between approximately 1.5 and 2 au. Just a few solar radii (R_\odot) from the Sun, a variety of techniques have revealed additional contributions to n_e that fall off very quickly with distance, scaling as r^{-4} , r^{-6} , or more steeply (Leblanc et al. 1998). These additional power-law components of the radial electron density profile will only prove important for describing observations where the LOS comes within just a few degrees of the Sun. NANOGrav observations are never intentionally taken while a pulsar is particularly close to the Sun, so only a small fraction of our data could be coincidentally influenced by these regions of the SW. As such, we do not model regions of non-inverse-square scaling in this work.

The SW is known to have strong latitudinal variation (Issautier et al. 1997). Near the solar activity minimum, for $|\beta| \lesssim 20^\circ$, the wind is relatively slow, producing a high electron density; the wind speed can vary a great deal with small variations of β in this equatorial region. Further poleward, the wind is faster, producing lower electron densities, and is more nearly constant in β . You et al. (2007) developed and built into TEMPO2 a DM model for the purpose of pulsar timing that incorporated both the fast and slow winds. There is some evidence for asymmetry between the northern and southern poleward winds based on in situ measurements taken with the *Ulysses* space probe, but the apparent asymmetry may be caused by evolution of the wind during the year the probe took to travel from one pole to the other (Issautier et al. 2004; Issautier et al. 2008).

To capture all of the known latitudinal structure in the wind, we would have to include large values of l in our model. We opt to not do so and consider only models with $l = 0$ and, consequently, $m = 0$. To demonstrate why we do this, define

$$\mathcal{Z}_l(t, \lambda, \beta) = \sqrt{4\pi} \int_{\hat{n}(t)} Y_{l0}(\lambda, \beta) \left(\frac{1 \text{ au}}{r}\right)^2 dl. \quad (3)$$

These functions encode the temporal structure of DM fluctuations attributable to moments of the SW's shape of various degrees l . We show several examples of \mathcal{Z}_l in Figure 1. There is a narrow window of orbital phase when the Sun and pulsar are near conjunction in which moments with different l can be differentiated from one another, and the amplitude of the signal falls off quickly as $|\beta|$ increases. Our data are not ideally suited for differentiating moments of different l for two reasons: we do not sample the narrow window of orbital phase near conjunction densely enough given our approximately monthly observing cadence, and only a small number of pulsars in our array are particularly close to the ecliptic.

Issautier et al. (2004) show that the primary change in the SW over the solar cycle is that the dense wind, constrained to $|\beta| \lesssim 20^\circ$ near the minimum of the solar activity cycle, spreads poleward, to as high as $|\beta| \approx 70^\circ$ during the solar activity

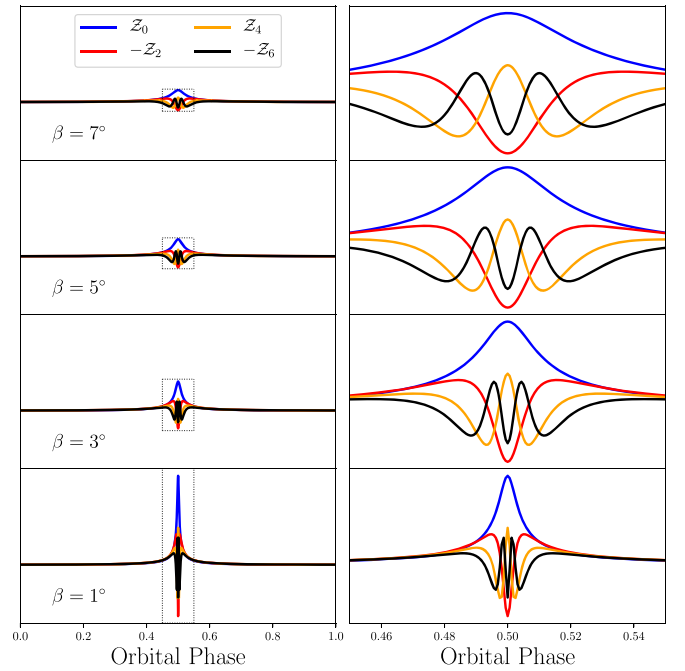


Figure 1. Time evolution of DM fluctuations caused by solar electron clouds shaped like $m = 0$ spherical harmonics of different degree l for pulsars at a variety of low ecliptic latitudes. The four curves in each panel correspond to different values of l . We have alternated the signs of the basis functions, i.e., we show positive \mathcal{Z}_0 and negative \mathcal{Z}_2 , and so on, because the sign of spherical harmonics at the equator alternates as such. The amplitude of the signal decreases quickly with increasing β (increasing as one moves upward through the panels). The panels on the left are all the same scale and show the entirety of one orbit. The panels on the right are magnifications of the black dotted boxes on the left.

maximum. To encapsulate this sort of time evolution in our model, we would have to incorporate moments with $l > 0$. We do not consider $l > 0$ for the reasons stated above, but we nonetheless consider variability in time in some of our modeling.

After these simplifications, our minimal model for the electron density in the SW is

$$n_\odot(t, r, \lambda, \beta) = n_\odot(r) = n_0(t) \left(\frac{1 \text{ au}}{r}\right)^2, \quad (4)$$

where $n_0(t)$ is the electron number density at 1 au. The component of DM that can be attributed to electrons in the solar electron cloud is $\mathcal{W}(t_i) = n_0(t) \mathcal{Z}_0(t_i, \lambda, \beta)$. This model treats the SW as diffuse and cold. Electron number densities in the wind make the plasma frequency much lower than typical observing frequencies. Electron velocities in the cloud are sufficiently nonrelativistic that the wind can be treated as cold. For all pulsars, \mathcal{Z}_0 depends exclusively on the geometry of the Earth–Sun–pulsar system, which is precisely measured through timing measurements.

In the frequency domain, fluctuations in DM from the SW appear with a fundamental frequency of 1 yr^{-1} . The phase of the signature is known. As the ecliptic latitude of a pulsar approaches zero, the duty cycle of the periodic SW signature becomes smaller, or the signature becomes more peaked (see Figure 1). This transfers power from the fundamental frequency

into higher harmonics. In the coming discussion, we demonstrate that the ISM can produce similar periodic fluctuations with high harmonic content, but that with an entire array of pulsars, the signatures can be disentangled.

3.2. The ISM

The ISM is an inhomogeneous medium with ionized density structures following an approximately Kolomogorov scaling law; that is, the power spectrum of spatial wave numbers, q , is proportional to $q^{-\kappa}$ with $\kappa \approx 11/3$ (Armstrong et al. 1995). Embedded in this turbulent Kolmogorov medium, there are discrete density structures such as magnetically collimated filaments and plasma lenses that can cause DM variation events and additional chromatic timing behavior inconsistent with the expectations of a Kolomogorov medium (e.g., Coles et al. 2015; Lam et al. 2018b). We do not incorporate such structures into our modeling because these discrete structures appear only rarely.

To model the influence of the turbulent ISM on observations of pulsars, material in the ISM is commonly described as being confined to a thin screen between the Earth and pulsar, transverse to the LOS. Using the techniques of Cordes et al. (2016), we have simulated the electromagnetic phase perturbation, ϕ , generated by propagation of light through thin screens of a Kolomogorov medium; phase perturbations $\phi(t)$ are related to DM perturbations as $\mathcal{D}(t) = -\nu\phi(t)/(c r_e)$, where c is the speed of light and r_e is the classical electron radius (Rickett 1990).

The trajectory that the LOS cuts through a screen depends on the distance of the screen and pulsar from the solar system barycenter (SSB), D_s and D_p respectively. The ecliptic coordinates and proper motion of the pulsar also affect the trajectory. For simplicity, we will assume that the screen is at rest relative to the SSB. Further, assume the Earth's orbit, $\mathbf{x}_e(t)$, is circular and perfectly confined to the ecliptic:

$$\mathbf{x}_e(t) = D_1 \begin{bmatrix} \cos[\omega_1(t - t_R)] \\ \sin[\omega_1(t - t_R)] \\ 0 \end{bmatrix} \quad (5)$$

where $\omega_1 = 2\pi \text{ yr}^{-1}$, $D_1 = 1 \text{ au}$, and t_R is a reference epoch, specifically an autumnal equinox.

At some reference epoch, t_0 , the position of a pulsar relative to the SSB is

$$\mathbf{x}_p(t_0) = D_p \begin{bmatrix} \cos \lambda_0 \cos \beta_0 \\ \sin \lambda_0 \cos \beta_0 \\ \sin \beta_0 \end{bmatrix}, \quad (6)$$

where λ_0 and β_0 are the pulsar's ecliptic longitude and latitude at t_0 , respectively. Since accelerations are small, we ignore them and take the rates of change of the pulsar's ecliptic coordinates as $\dot{\beta} = \mu_\beta$ and $\dot{\lambda} = \mu_\lambda / \cos \beta$, where μ_β and μ_λ are the components of the pulsar's proper motion in ecliptic coordinates. We model the ecliptic coordinates as functions of time as $\beta(t) = \beta_0 + \dot{\beta}t$ and $\lambda(t) = \lambda_0 + \dot{\lambda}t$.

Define $\hat{\mathbf{X}}$ and $\hat{\mathbf{Y}}$, orthogonal vectors spanning planes transverse to the line connecting the SSB and the position of

the pulsar at t_0 :

$$\hat{\mathbf{X}} = \begin{bmatrix} \sin \lambda_0 \\ -\cos \lambda_0 \\ 0 \end{bmatrix}, \quad (7)$$

$$\hat{\mathbf{Y}} = \begin{bmatrix} -\cos \lambda_0 \sin \beta_0 \\ -\sin \lambda_0 \sin \beta_0 \\ \cos \beta_0 \end{bmatrix}. \quad (8)$$

We specify positions in the screen with coordinates ΔX and ΔY along $\hat{\mathbf{X}}$ and $\hat{\mathbf{Y}}$, respectively. It can be shown that

$$\mathbf{x}_p(t) \approx \mathbf{x}_p(t_0) - \mu_\lambda D_p(t - t_0)\hat{\mathbf{X}} + \mu_\beta D_p(t - t_0)\hat{\mathbf{Y}}. \quad (9)$$

If $D_s \gg D_1$, the location at which the LOS intersects the screen will be

$$\mathbf{x}_s(t) \approx \frac{D_s}{D_p}\mathbf{x}_p(t) + \left(1 - \frac{D_s}{D_p}\right)\mathbf{x}_e(t). \quad (10)$$

Projected onto the basis spanning the screen,

$$\begin{aligned} \mathbf{x}_s(t) \cdot \hat{\mathbf{X}} &\approx -D_s \mu_\lambda (t - t_0) \\ &\quad - D_1 \left(1 - \frac{D_s}{D_p}\right) \sin[\omega_1(t - t_R) - \lambda_0], \end{aligned} \quad (11)$$

and

$$\begin{aligned} \mathbf{x}_s(t) \cdot \hat{\mathbf{Y}} &\approx D_s \mu_\beta (t - t_0) \\ &\quad - D_1 \sin \beta_0 \left(1 - \frac{D_s}{D_p}\right) \cos[\omega_1(t - t_R) - \lambda_0]. \end{aligned} \quad (12)$$

In each component of the screen trajectory, there is one term that grows linearly in time and is proportional to the product of D_s and a component of proper motion; the other term oscillates annually and has a larger amplitude for smaller values of D_s . The relative scale of these two terms influences the qualitative shape of the trajectory the LOS cuts through the screen and, consequently, the spectral properties of the DM fluctuations caused by sampling the screen along that trajectory. This is demonstrated in Figures 2 and 3.

In the top panel of Figure 2 we depict the trajectory the LOS tracks across screens placed at different distances from the Earth for J0030+0451. The bottom left panel of Figure 2 shows those three different trajectories projected onto a single realization of a Kolomogorov phase screen. The bottom right panel shows the value of ϕ from the phase screen evaluated along those trajectories (color coded). The nearest screen yields fluctuations in ϕ that are noticeably quasiperiodic with an approximately annual fundamental periodicity. As the screen distance is increased, this quasiperiodicity begins to vanish. Figure 3 maps out the influence of D_s on the spectral properties of fluctuations in ϕ . We vary D_s between 1% and 99% of D_p , sample ϕ along the trajectory the LOS cuts through the screen, and compute the modulus of the Fourier transform of the resultant time series, $|\mathcal{F}(\phi)|$. The surfaces in Figure 3 show the results of this calculation averaged over 100 screen realizations for PSRs J0030+0451 and J1614–2230.

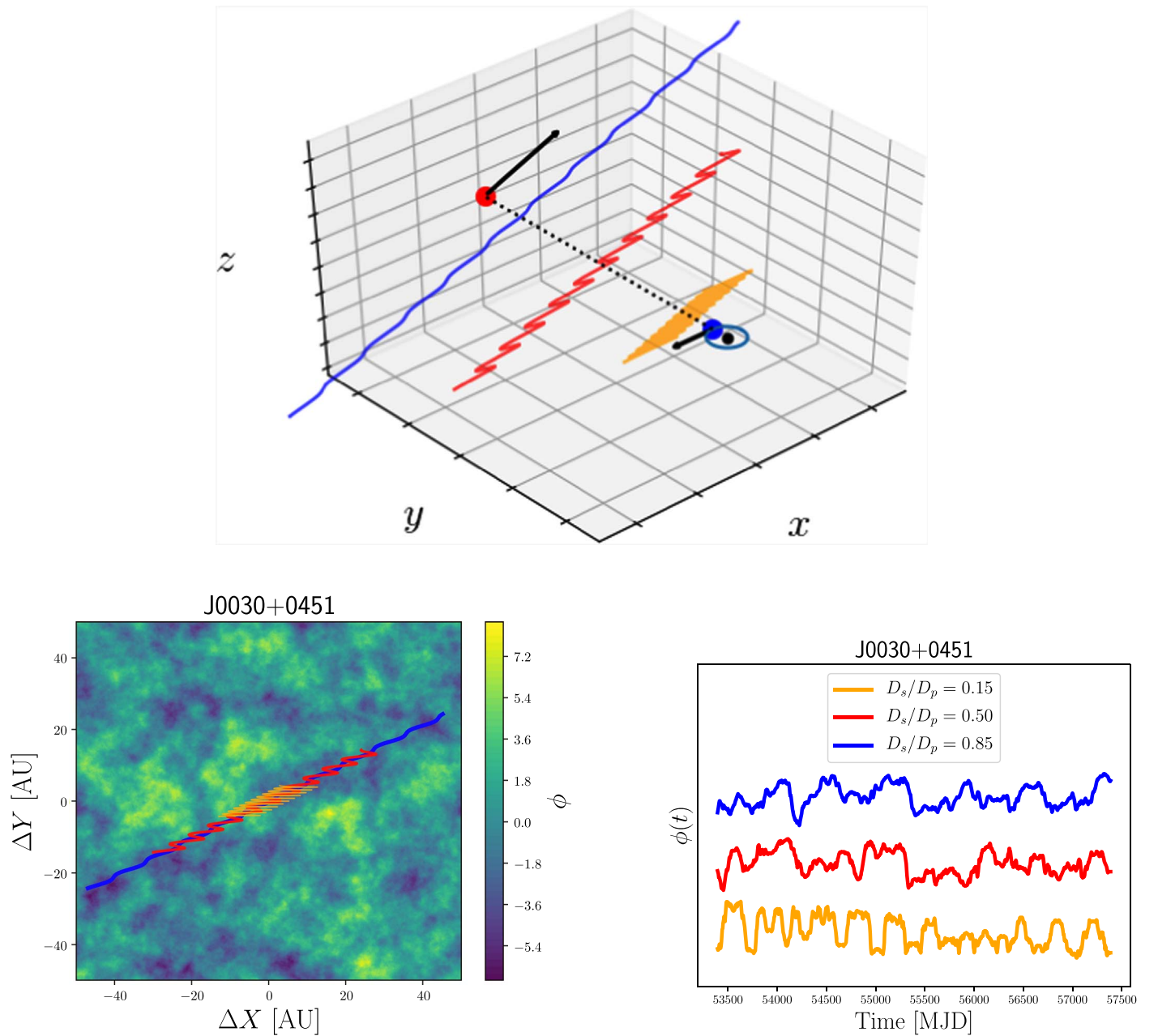


Figure 2. Top: the Earth (blue dot) orbits the solar system barycenter (black dot), and the pulsar (red dot) displays proper motion transverse to the LOS. The orange, red, and blue curves represent the trajectory the LOS cuts through transverse planes at varying distances between the Earth and pulsar (not to scale). These curves were generated using the ecliptic coordinates and proper motion for J0030+0451. Bottom left: a Kolomogorov phase perturbation screen and the trajectory traced through the screen if it is placed at different distances between the Earth and pulsar. Bottom right: the phase perturbation from the Kolomogorov screen sampled along the three different trajectories. The nearest screen (orange) leads to quasiperiodic fluctuations in ϕ . This quasiperiodicity is noticeably reduced for more distant screens. The vertical offset between the curves is put in by hand for visual clarity.

The results in Figure 3 are qualitatively different for the two pulsars. The magnitude of proper motion for J0030+0451 is approximately 6 mas yr^{-1} , substantially smaller than the proper motion of J1614–2230, which is approximately 32 mas yr^{-1} . Additionally, the distance to J0030+0451 is approximately 0.3 kpc , as opposed to 0.65 kpc for J1614–2230 (Matthews et al. 2016). Since J0030+0451 is closer than J1614–2230 and has less proper motion, the linearly growing terms in Equations (11) and (12) are typically less significant for J0030+0451, making the annual terms more important. These statements about the shape of the trajectories the LOS cuts

through screens, when mapped to the spectral properties of temporal variations in ϕ , mean that one expects J0030+0451 to show more quasiperiodic variation from the ISM than J1614–2230. For $D_s \lesssim 0.1 \text{ kpc}$, J0030+0451 displays strong fluctuations at approximately 1 yr^{-1} with additional power at numerous higher harmonics. J1614–2230 is relatively free from such quasiperiodicity. The low-frequency “red” power (more power at lower frequencies) visible for all but the lowest values of D_s is associated with the linear terms in Equations (11) and (12), stochastic fluctuations caused by the sampling region drifting across a Kolomogorov screen.

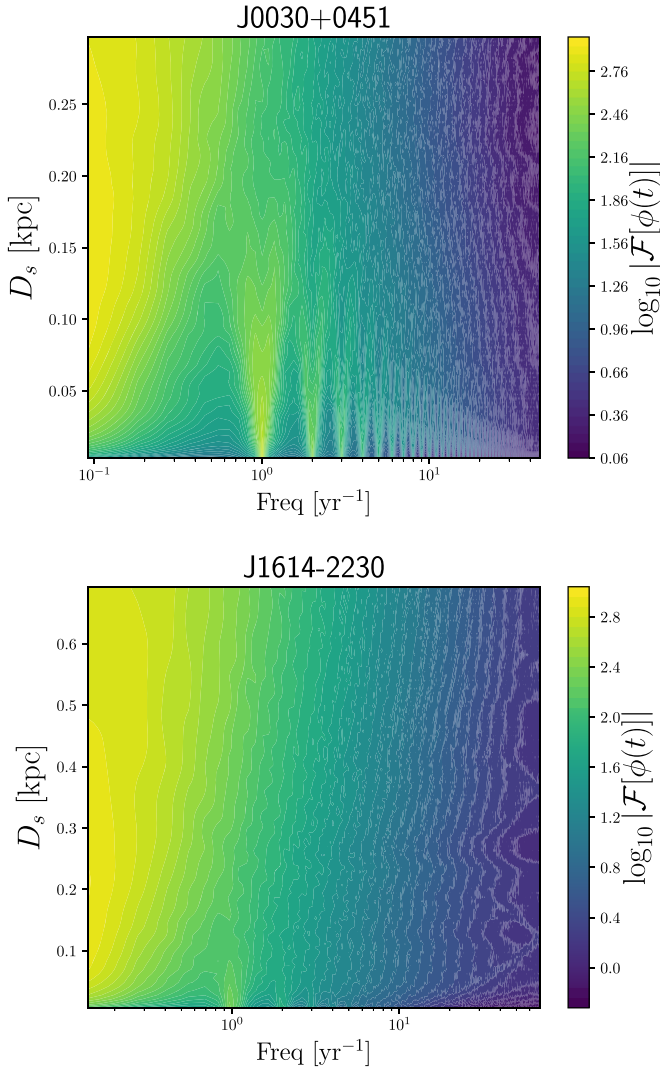


Figure 3. Anticipated spectral power in DM fluctuations from screens at varied distances from the SSB D_s , for two example pulsars with low ecliptic latitudes. The position, proper motion, and distance of a pulsar strongly influence the anticipated result. J0030+0451, a nearby, low-proper-motion pulsar, can show pronounced quasiperiodic fluctuations for sufficiently close screens. Faster moving and more distant J1614–2230 is less prone to such quasiperiodic fluctuations. The low-frequency fluctuation power is a feature common to all pulsars; it is associated with sampling distinct regions of the screen over time.

4. Implementation

We describe our DM time series as a superposition of SW and ISM contributions, \mathcal{W} and \mathcal{I} , respectively:

$$\mathcal{D}_0 + \delta\mathcal{D} = \mathcal{W} + \mathcal{I}. \quad (13)$$

Based on our analysis in Section 3.2, we further subdivide \mathcal{I} into the sum of two terms: \mathcal{R} , a stochastic red process confined to frequencies below 1 yr^{-1} , and \mathcal{P} , a periodic sinusoid of unspecified amplitude and phase with a frequency of 1 yr^{-1} . This is, of course, an approximate description. The low-frequency red power extends to frequencies above 1 yr^{-1} , but specifically because it is red, power in those higher frequencies will be subdominant. Power in the fundamental harmonic of the quasiperiodic oscillations can be at frequencies near, but not at, 1 yr^{-1} . Additionally, harmonics of 1 yr^{-1} may be present in the quasiperiodic signals associated with the ISM. We ignore these

higher harmonics in our description of \mathcal{I} because they contain less power than the fundamental and they only matter if there are very nearby screens between Earth and pulsars with low proper motion.

Our aim in this work is to make inferences about the SW with our DM measurements. From this perspective, the SW signal is contaminated by the ISM signal, part of which, \mathcal{R} , is stochastic and red. To mitigate \mathcal{R} , we perform a weighted Gaussian convolution to separate our DM time series $\delta\mathcal{D}$ into low-frequency and high-frequency contributions, $\delta\tilde{\mathcal{D}}$ and $\delta\tilde{\mathcal{D}}'$, respectively. In detail,

$$\delta\tilde{\mathcal{D}}(t_i) = \left[\sum_j w_{ij} \right]^{-1} \sum_j w_{ij} \delta\mathcal{D}(t_j), \quad (14)$$

where

$$w_{ij} = \frac{1}{\sigma_j^2} \exp \left[-\frac{(t_i - t_j)^2}{2\tau^2} \right], \quad (15)$$

and τ is a smoothing timescale. This defines a linear operator \mathbf{L} such that $\delta\tilde{\mathcal{D}} = \mathbf{L}\delta\mathcal{D}$. Also define $\mathbf{H} = \mathbf{I} - \mathbf{L}$ where \mathbf{I} is the identity matrix. Then $\delta\tilde{\mathcal{D}} = \mathbf{H}\delta\mathcal{D}$. Note that the nominal DM, \mathcal{D}_0 , is a constant signal, so $\mathbf{L}\mathcal{D}_0 = \mathcal{D}_0$ and $\mathbf{H}\mathcal{D}_0 = 0$.

We have fixed the timescale $\tau = \sqrt{2 \log 2} / \pi \text{ yr}$; convolution of a time series with a Gaussian of width τ is equivalent to multiplying the Fourier transform of that time series by a Gaussian centered at zero with a half-width at half-maximum of 0.5 yr^{-1} . Power at frequencies above 0.5 yr^{-1} is strongly attenuated, making $\delta\tilde{\mathcal{D}}$ a smoothed version of $\delta\mathcal{D}$ largely devoid of periodic signals with frequencies at or above 1 yr^{-1} .

We choose the above value of τ so that $\mathbf{H}\mathcal{R} \approx 0$. In practice, we write $\mathcal{P} = a\mathcal{S} + b\mathcal{C}$, a linear combination of an annual sinusoid, $\mathcal{S} = \sin[\omega_1(t - t_R)]$, and cosinusoid, $\mathcal{C} = \cos[\omega_1(t - t_R)]$, of unspecified amplitudes a and b . This can alternatively be parameterized as $\mathcal{P} = A \cos[\omega_1(t - t_R) - \Phi]$, where $A^2 = a^2 + b^2$ and $\Phi = \arctan 2(a, b)$. Multiplying Equation (13) through by \mathbf{H} yields

$$\begin{aligned} \delta\tilde{\mathcal{D}} &= \mathbf{H}(\mathcal{W} + \mathcal{P} + \mathcal{R}), \\ &\approx n_0(t)\tilde{\mathcal{Z}}_0 + a\tilde{\mathcal{S}} + b\tilde{\mathcal{C}}, \end{aligned} \quad (16)$$

where $\tilde{\mathcal{Z}}_0 = \mathbf{H}\mathcal{Z}_0$, and $\tilde{\mathcal{S}}$ and $\tilde{\mathcal{C}}$ are similarly defined. As a reminder, \mathcal{Z}_0 is defined by Equation (3). Though \mathcal{Z}_0 , \mathcal{S} , and \mathcal{C} primarily consist of power at or above frequencies of 1 yr^{-1} , they are somewhat modified by the high-pass filter \mathbf{H} . To quantify that modification, define $\Delta\mathcal{Z}_0 = \mathcal{Z}_0 - \tilde{\mathcal{Z}}_0$. Similarly, define $\Delta\mathcal{S}$ and $\Delta\mathcal{C}$. These corrections are useful because they connect idealized basis elements like \mathcal{Z}_0 to their filtered counterparts ($\tilde{\mathcal{Z}}_0$ in this case), which depend on the data.

Consider the simple case where n_0 is constant. In this case, we model the \mathbf{H} -filtered DM time series for individual pulsars as a linear combination of three basis elements. We constrain the coefficients n_0 , a , and b with generalized least-squares techniques. Define a so-called “design matrix” $\mathbf{M} = [\tilde{\mathcal{Z}}_0, \tilde{\mathcal{S}}, \tilde{\mathcal{C}}]$. Then the best-fit values for the coefficients are

$$\begin{bmatrix} \hat{n}_0 \\ \hat{a} \\ \hat{b} \end{bmatrix} = (\mathbf{M}^T \mathbf{\Xi}^{-1} \mathbf{M})^{-1} \mathbf{M}^T \mathbf{\Xi}^{-1} \delta\tilde{\mathcal{D}}, \quad (17)$$

where Ξ^{-1} was defined in Section 2. A least-squares analysis like this has been done in this context before. Splaver et al. (2005), in a study of PSR J1713+0747, found $\hat{n}_0 = 5 \pm 4 \text{ cm}^{-3}$. In a similar study of PSR J0030+0451, a pulsar much nearer the ecliptic than J1713+0747, Lommen et al. (2006) found $\hat{n}_0 = 6.9 \pm 2.1 \text{ cm}^{-3}$. Both authors assumed a constant value for n_0 , so we will consider that case as well for comparison, but neither attempted to mitigate the stochastic low-frequency or periodic signatures potentially produced by the ISM.

The NANOGrav 11 yr data set contains DM time series for $N = 45$ pulsars, and we can leverage the whole data set to constrain n_0 . To this end, we append an index to our basis elements to indicate which pulsar in the array we are referring to; for example, $\tilde{\mathcal{Z}}_{0,1}$, $\tilde{\mathcal{S}}_1$, and $\tilde{\mathcal{C}}_1$ correspond to the first pulsar in our array. Define a global design matrix

$$\mathbf{M}_G = \begin{bmatrix} \tilde{\mathcal{Z}}_{0,1} & \tilde{\mathcal{S}}_1 & \tilde{\mathcal{C}}_1 & 0 & 0 & \cdots & 0 & 0 \\ \tilde{\mathcal{Z}}_{0,2} & 0 & 0 & \tilde{\mathcal{S}}_2 & \tilde{\mathcal{C}}_2 & \cdots & 0 & 0 \\ \vdots & \vdots & \vdots & \vdots & \vdots & \ddots & \vdots & \vdots \\ \tilde{\mathcal{Z}}_{0,N} & 0 & 0 & 0 & 0 & \cdots & \tilde{\mathcal{S}}_N & \tilde{\mathcal{C}}_N \end{bmatrix}. \quad (18)$$

There are $2N + 1$ columns in \mathbf{M}_G , and the number of rows is the total number of DM measurements summed over all pulsars,²⁵ $N_{\text{DM}} = 3321$. Similarly, define a block-diagonal global inverse covariance matrix

$$\Xi_G^{-1} = \begin{bmatrix} \Xi_1^{-1} & \cdots & 0 \\ \vdots & \ddots & \vdots \\ 0 & \cdots & \Xi_N^{-1} \end{bmatrix}. \quad (19)$$

Then

$$\begin{bmatrix} \hat{n}_0 \\ \hat{a}_1 \\ \hat{b}_1 \\ \vdots \\ \hat{a}_N \\ \hat{b}_N \end{bmatrix} = \mathbf{C}_{p,G} \mathbf{M}_G^T \Xi_G^{-1} \delta \tilde{\mathcal{D}}_G, \quad (20)$$

where $\delta \tilde{\mathcal{D}}_G^T = [\delta \tilde{\mathcal{D}}_1^T \cdots \delta \tilde{\mathcal{D}}_N^T]$ and the global parameter covariance matrix $\mathbf{C}_{p,G} = (\mathbf{M}_G^T \Xi_G^{-1} \mathbf{M}_G)^{-1}$.

With a slight elaboration of this least-squares framework, we also test for variations in n_0 over time. We define a grid of $N_T = 13$ times T_i with 1 yr spacing; the latest of them is MJD 53788—one day after the final observation in the 11 yr data set—and the earliest is precisely 12 yr earlier, spanning the full 11 yr data set (which actually spans approximately 11.4 yr). We treat n_0 as piecewise constant between grid points, meaning we allow it to take on $N_T - 1 = 12$ different values. Rather than a single basis element \mathcal{Z}_0 being used to describe SW fluctuations, we now use $N_T - 1$ basis elements $\mathcal{Z}_0(T_i, T_{i+1})$ that are equal to \mathcal{Z}_0 between T_i and T_{i+1} and zero otherwise. These are then high-pass filtered to produce $\tilde{\mathcal{Z}}_0(T_i, T_{i+1})$. The solar basis elements are then stacked into the first $N_T - 1$ columns of \mathbf{M}_G .

²⁵ For PSR J1713+0747, we removed 11 DM measurements between MJDs 54710 and 55080. During this time, there was an extreme scattering event observed in this pulsar, causing DM evolution not describable within our framework (Lam et al. 2018b).

5. Results

Our final model for the DM variations in a pulsar is

$$\delta \mathcal{D}_M = \delta \tilde{\mathcal{D}} + \hat{n}_0 \tilde{\mathcal{Z}}_0 + \hat{a} \tilde{\mathcal{S}} + \hat{b} \tilde{\mathcal{C}}. \quad (21)$$

We first consider the case where n_0 is constant. After carrying out the analysis described above, the values of \hat{a} and \hat{b} for each of the 45 pulsars in the NANOGrav 11 yr data set, along with their uncertainties, are given in Table 1. As noted above, the annual DM fluctuations from the ISM, $\mathcal{P} = a\mathcal{S} + b\mathcal{C}$, can alternatively be parameterized as $\mathcal{P} = A \cos[\omega_1(t - t_R) - \Phi]$ with $A^2 = a^2 + b^2$ and $\Phi = \arctan 2(a, b)$. We also give best-fit values of these parameters, \hat{A} and $\hat{\Phi}$, in Table 1. The ability to differentiate the annual DM fluctuations caused by structure in the ISM from those caused by the SW is greatly facilitated by the techniques developed in this work, relying on the many lines of sight made accessible by a full pulsar timing array.

Our best-fit value for the electron density in the SW at 1 au when it is assumed to be constant is $\hat{n}_0 = 7.9 \pm 0.2 \text{ cm}^{-3}$. The default value of n_0 used by TEMPO2 is 4 cm^{-3} ; the default value used by TEMPO is 10 cm^{-3} (Edwards et al. 2006; Nice et al. 2015). Our result indicates that the default model for the SW in TEMPO2 will underestimate dispersive delays, while TEMPO will overestimate them.

We can compare our result for \hat{n}_0 to a long line of pulsar-based inferences about the SW. Goldstein & Meisel (1969) observed the Crab Pulsar with the old 300 foot telescope of the National Radio Astronomy Observatory in Green Bank during an occultation by the solar corona and failed to successfully detect variations in DM from the SW at all. With the more sensitive Arecibo telescope and using timing techniques more closely resembling those used today, Counselman & Rankin (1972) observed the Crab Pulsar through occultation in 1969 and 1970. They not only detected DM variations from the SW,²⁶ but also found that between 5 and 20 solar radii, the SW was not yet free-streaming, and the electron density to radius relation scales with an exponent of -2.9 ± 0.2 . As we have discussed, in a study of PSR J1713+0747, Splaver et al. (2005) found $n_0 = 5 \pm 4 \text{ cm}^{-3}$, which is a marginal detection. In a study of PSR J0030+0451, with an ecliptic latitude of approximately 1.5° (the ecliptic latitude of PSR J1713+0747 is approximately 30°), Lommen et al. (2006) measured $n_0 = 6.9 \pm 2.1 \text{ cm}^{-3}$. The results from Splaver et al. (2005) and Lommen et al. (2006) are consistent with our result; our much-increased precision is attributable to improvements in hardware at Arecibo and GBT (DuPlain et al. 2008; Ransom et al. 2009) and to the techniques we have developed here to combine measurements from many pulsars. Furthermore, our techniques allow us to mitigate potential bias in SW measurements caused by annual fluctuations in DM from the ISM.

In Figures 4 and 5, we show the results of our modeling in detail for two pulsars: J1614–2230, the NANOGrav pulsar closest to the ecliptic, and J1909–3744, arguably the single best timed of the NANOGrav pulsars (Lam et al. 2018a).

The model residuals for J1614–2230 in Figure 4 show no obvious structure. The most visible outlier (though it is within

²⁶ Counselman & Rankin (1972) measured the electron density of the SW at $10 R_\odot$ to be $7000 \pm 600 \text{ cm}^{-3}$. Given the non-inverse-square scaling of the electron density they found within $20 R_\odot$ and that is known to exist from other studies, it is not straightforward to compare their measured electron density to ours, which we have referenced to 1 au.

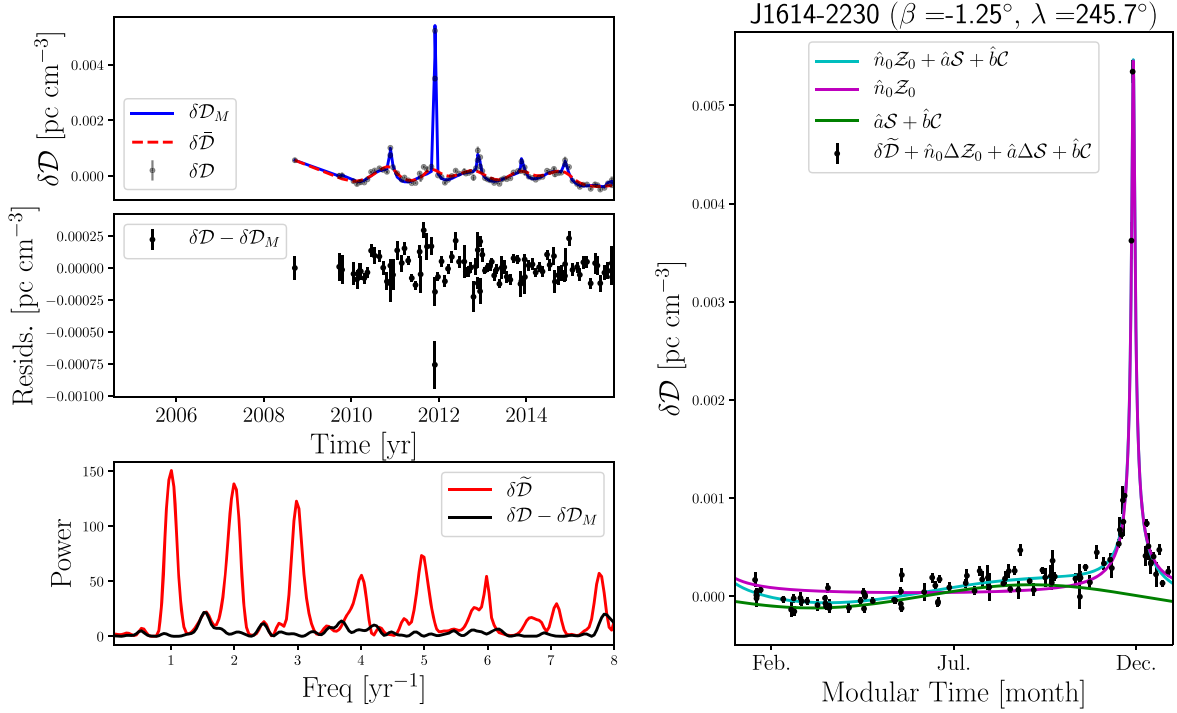


Figure 4. Modeling results as applied to PSR J1614–2230. Top left: Measured variations in DM about a nominal value, $\delta\mathcal{D}$, are shown as black dots. The dashed red curve is a low-frequency approximation to the DM fluctuations, $\delta\tilde{\mathcal{D}}$, the result of convolving $\delta\mathcal{D}$ with a Gaussian (see Equations (14) and (15)). The blue curve represents the best-fit model, $\delta\mathcal{D}_M$, as described in Equation (21). Middle left: model residuals, i.e., $\delta\mathcal{D} - \delta\mathcal{D}_M$. Bottom left: unnormalized Lomb–Scargle periodograms of the high-frequency component of the DM fluctuations, $\delta\tilde{\mathcal{D}}$, and the residuals, $\delta\mathcal{D} - \delta\mathcal{D}_M$. Right: The black dots are the high-pass filtered DM data plotted modulo 1 yr; we have added the basis corrections $\Delta\mathcal{Z}_0$, $\Delta\mathcal{S}$, and $\Delta\mathcal{C}$ scaled by the best-fit coefficients \hat{n}_0 , \hat{a} , and \hat{b} to compare the filtered DM data and the basis functions \mathcal{Z}_0 , \mathcal{S} , and \mathcal{C} (see the discussion following Equation (16)). The green (magenta) curve is the best-fit contribution from the ISM (SW). The cyan curve is the sum of the magenta and green curves.

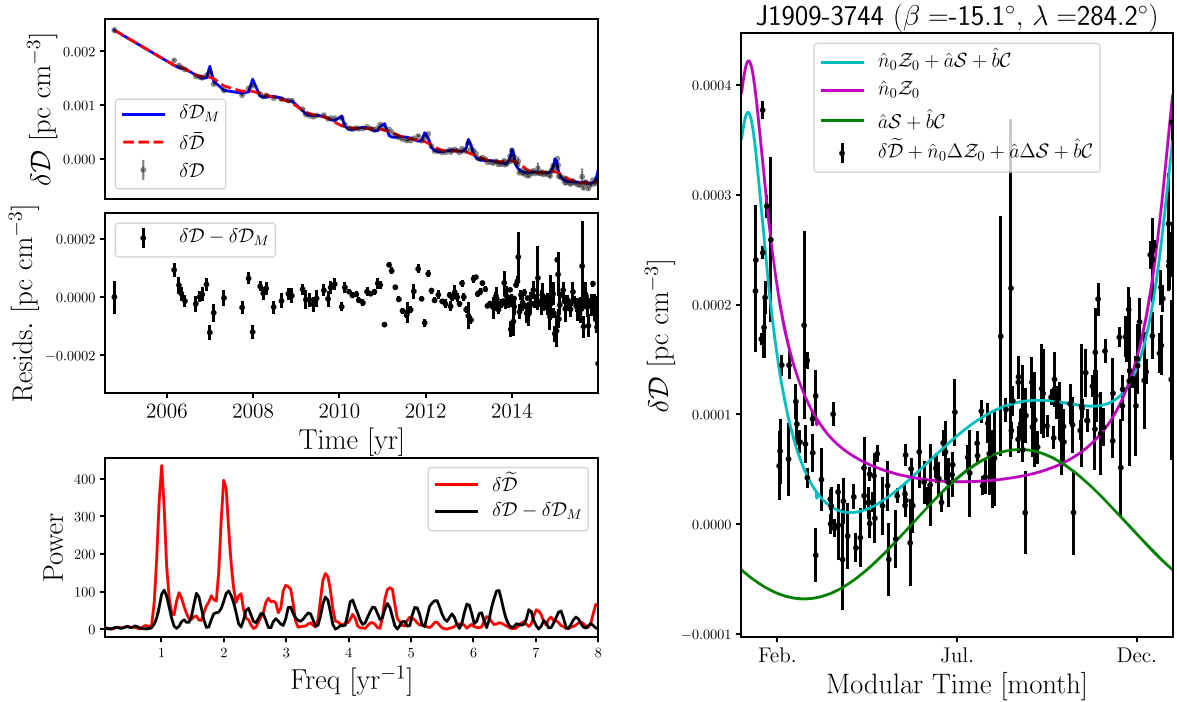


Figure 5. As in Figure 4, but for PSR J1909–3744.

4σ of zero) is associated with the observation taken *second* closest to the Sun. It is possible that we cannot satisfactorily model both of the two closest observations to the Sun for this pulsar without considering non-inverse-square components of

the SW. It is also possible that a discrete event such as a coronal mass ejection influenced this individual measurement, as was the case in Howard et al. (2016); for observations taken so close to the Sun, such considerations may become

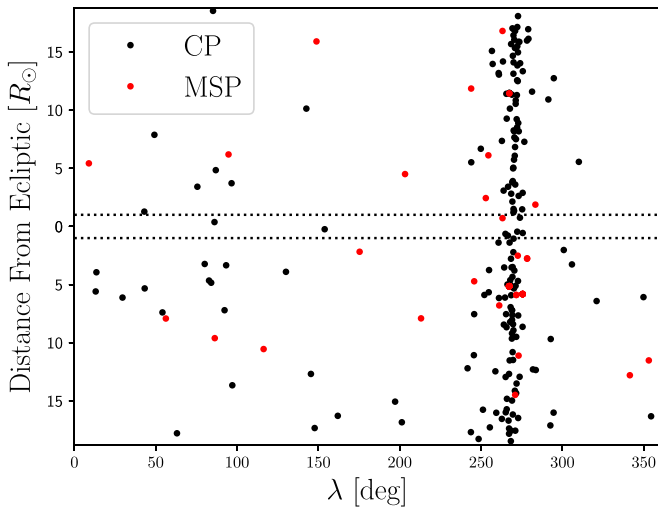


Figure 6. All pulsars with $|\beta| \leq 5^\circ$ according to the Australian Telescope National Facility (ATNF) pulsar catalog (Manchester et al. 2005). The lines of sight to these pulsars come within 20 solar radii of the Sun (as indicated by the y axis). The dense vertical strip of pulsars near $\lambda = 270^\circ$ are in the direction of the Galactic interior and approach the Sun around December or January of every year. The red dots represent millisecond pulsars (MSP), and the black dots represent canonical pulsars (CP). The horizontal dashed line represents the angular extent of the Sun.

important. In the periodogram,²⁷ it is clear that the many harmonics of 1 yr^{-1} present in the DM fluctuations of this pulsar have been successfully mitigated.

The model residuals for J1909–3744 in Figure 5 show much more structure than those of J1614–2230 in Figure 4. It is possible that this is an unmodeled influence of the ISM. J1909–3744 has a high proper motion (Matthews et al. 2016), which we argue tends to reduce the periodic content of ISM-induced DM fluctuations. However, the right panel of Figure 5 shows a clear “shoulder” in this pulsar’s annual DM fluctuations that is well fit by the green curve describing an annual sinusoid from the ISM. This may indicate a screen of ISM material between Earth and J1909–3744 that is very close to the solar system. Additionally, Figure 1 shows that for pulsars farther from the ecliptic, though the perturbation to DM from the SW is smaller in amplitude, it is spread out over a bigger percentage of orbital phase. It is possible that our observing cadence is high enough and the DM measurement precision for J1909–3744 is good enough that unmodeled latitudinal structure in the SW is showing up in the model residuals.

When we relax the requirement that n_0 be constant throughout our data set and allow it to be piecewise constant, as discussed at the end of the previous section, we get the results shown in Figure 6. Although we allowed n_0 to take on a different value in each of the 12 yr that the 11 yr data set spills into, we only show the results for the final 10 yr. The first value of n_0 we exclude from the plot is $1.9 \pm 4.6 \text{ cm}^{-3}$: only 18 of the 3321 DM measurements we used fall into the span of times constraining this first value of n_0 , only 11 of our 45 pulsars have data going that far back in time, and all but two of those pulsars are more than 10° from the ecliptic. The second value we exclude from the plot is $-2.5 \pm 1.7 \text{ cm}^{-3}$. Our fitting procedure does not restrict n_0 to positive values, but only

positive values are physically meaningful. Only 62 DM measurements from just 18 pulsars are used to determine this value of n_0 , but just 11 of those DM measurements are from the three pulsars within 10° of the ecliptic. But the main issue with this second excluded value is that it is centered on a year where the GBT was off-line for much of the year, leaving almost a year-long gap in our observations of many pulsars. Both early values excluded from Figure 6 are within 2σ of zero, consistent with nondetections of the SW.

Figure 6 shows clear improvement in measurement precision over time as more pulsars were added to the NANOGrav timing program and hardware at our telescopes was upgraded. All best-fit values of n_0 when it is allowed to vary from year to year (except the early negative value coincident with the year-long shutdown of the GBT) are within 3σ of 7.9 cm^{-3} , the best-fit value of n_0 when it is assumed to be constant throughout our full data span (as indicated by the dotted black line with 1σ uncertainty shaded in red in Figure 6). Though there was a minimum in solar activity²⁸ around 2008 that grew toward a maximum around 2013—a trend that can potentially be seen in Figure 6—our data set is not sensitive enough to definitively say we detect temporal variation in the SW.

Table 2 summarizes our results by presenting χ^2 values for various steps of our modeling on a pulsar-by-pulsar basis. If \mathcal{Q} are the residuals of a particular model, $\chi^2 = \mathcal{Q}^T \Xi^{-1} \mathcal{Q}$. We have divided the χ^2 values by N_{obs} , the number of DM observations for a pulsar. This is approximately equal to the number of degrees of freedom for that pulsar, but straightforwardly determining the number of degrees of freedom for a particular pulsar is complicated by the nature of our modeling. The filtering we do is not equivalent to fitting out a parameterized model, and some of our fit parameters affect pulsars individually (an annual sine and cosine per pulsar), while some parameters affect all pulsars by varying amounts depending on the pulsar’s ecliptic latitude (a constant or piecewise constant n_0). For instances when we have fit out an annual sine and cosine per pulsar, we divide by $(N_{\text{obs}} - 2)$.

In Table 2, we include the sum of the N_{obs} and all χ^2 columns. These sums show that high-pass filtering dramatically reduces the global χ^2 , an annual sine and cosine per pulsar plus a constant n_0 model further substantially reduces the global χ^2 , and a time variable n_0 reduces the global χ^2 marginally further. This picture of steady fit improvement at each subsequent step of our modeling is complicated when tested on a pulsar-by-pulsar basis. For J0030+0451, the pulsar second closest to the ecliptic in our sample, the χ^2 value improves at each step. For J1614–2230, the pulsar closest to the ecliptic in our sample, the constant n_0 model dramatically improves the χ^2 value as compared to the high-pass filtered case, but the χ^2 value is made marginally worse by allowing n_0 to vary. Notably, these pulsars probe different hemispheres of the SW, and we may just be seeing that time evolution without latitudinal variation is insufficient for modeling our most near-ecliptic pulsars. The high values of χ^2 for many pulsars indicate that our DM measurement uncertainties are very small and that there is structure left over in our DM time series from still-unmodeled phenomenology in the ISM and SW.

6. Prospects and Concluding Remarks

The NANOGrav 11 yr data set is among the best collections of pulsar timing data in existence for looking for and studying

²⁷ We have used the unnormalized Lomb–Scargle periodogram as described in Equation (12) of VanderPlas & Ivezić (2015) and implemented in Astropy (The Astropy Collaboration et al. 2018).

²⁸ www.swpc.noaa.gov/products/solar-cycle-progression

Table 2
 χ^2 Values for Different Models

PSR	β (deg)	N_{obs}	χ^2/N_{obs} No Model	χ^2/N_{obs} High Pass	$\chi^2/(N_{\text{obs}} - 2)$ Fix n_0	$\chi^2/(N_{\text{obs}} - 2)$ Vary n_0
J0023+0923	6.3	50	2527.9	1615.8	666.0	643.1
J0030+0451	1.4	102	738.6	715.0	107.5	76.8
J0340+4130	21.3	56	119.8	2.1	1.8	1.8
J0613-0200	-25.4	121	1281.7	20.3	12.0	12.2
J0636+5128	28.2	26	24.1	9.5	5.9	6.0
J0645+5158	28.8	61	18.2	11.0	10.4	10.4
J0740+6620	44.1	26	7.0	4.6	4.8	4.8
J0931-1902	-31.7	39	3.8	2.2	2.0	2.0
J1012+5307	38.7	123	45.3	3.6	3.5	3.5
J1024-0719	-16.0	82	81.4	4.0	3.0	3.1
J1125+7819	62.4	25	372.8	106.0	95.7	95.8
J1453+1902	33.9	22	5.4	6.7	6.9	6.9
J1455-3330	-16.0	108	21.6	9.5	8.3	8.6
J1600-3053	-10.0	106	612.2	15.5	9.5	9.7
J1614-2230	-1.2	92	311.0	260.2	6.6	5.8
J1640+2224	44.0	111	1788.6	84.3	72.6	77.5
J1643-1224	9.7	122	3061.2	62.1	57.5	56.1
J1713+0747	30.7	198	85.7	26.7	26.1	20.4
J1738+0333	26.8	54	181.3	9.5	9.0	9.1
J1741+1351	37.2	59	506.0	38.3	35.4	35.7
J1744-1134	11.8	116	300.7	53.9	44.6	47.8
J1747-4036	-17.2	54	138.1	11.6	11.1	11.1
J1832-0836	14.5	39	503.2	10.5	4.4	4.6
J1853+1303	35.7	53	253.8	292.1	292.6	292.1
B1855+09	32.3	101	2298.0	12.2	13.4	13.9
J1903+0327	25.9	60	1961.5	8.0	6.1	6.1
J1909-3744	-15.1	166	4013.2	27.5	15.8	15.0
J1910+1256	35.1	67	25.6	6.2	5.9	5.8
J1911+1347	35.8	25	165.5	5.2	1.5	1.6
J1918-0642	15.3	117	374.7	5.0	3.4	3.1
J1923+2515	46.6	48	51.1	25.8	20.3	20.9
B1937+21	42.2	165	22133.8	1118.3	1013.0	1025.7
J1944+0907	29.8	53	2376.1	36.4	29.7	29.6
B1953+29	48.6	47	363.7	78.2	79.4	79.3
J2010-1323	6.4	88	139.1	29.1	5.2	5.4
J2017+0603	25.0	49	43.2	16.9	7.6	7.8
J2033+1734	35.0	23	28.0	19.9	22.1	22.5
J2043+1711	33.9	65	652.2	271.5	227.2	225.9
J2145-0750	5.3	107	181.9	49.7	64.5	60.5
J2214+3000	37.7	53	32.5	38.0	32.1	32.2
J2229+2643	33.2	21	3.0	2.2	2.4	2.4
J2234+0611	14.0	23	17.8	5.8	5.5	5.4
J2234+0944	17.3	29	80.9	44.6	37.5	37.1
J2302+4442	45.6	58	23.6	8.4	8.6	8.7
J2317+1439	17.6	111	133009.7	244.9	217.7	184.9
SUM		3321	180966.6	5430.7	3318.0	3241.0

nanohertz gravitational waves, rivaled only by similar data sets from the European Pulsar Timing Array (Kramer & Champion 2013; Desvignes et al. 2016) and the Parkes Pulsar Timing Array (Hobbs 2013; Reardon et al. 2016). But if one set out to observe pulsars for the purpose of investigating the SW rather than gravitational waves, the set of pulsars observed and the observing strategies employed would be quite different.

Tiburzi & Verbiest (2018) recently presented low-frequency (approximately 100 MHz), high-cadence (approximately weekly) observations of three pulsars within 9° of the ecliptic conducted with individual stations of the Low-Frequency Array (LOFAR) telescope. Since dispersive timing delays scale as the inverse square of radio frequency, sensitivity to DM is greatly improved

at these low observing frequencies. As Figure 1 shows, high-cadence observations, particularly through solar conjunction, are necessary for probing latitudinal variations in the SW; higher than weekly cadence would be beneficial within approximately 10 days before and after solar conjunction.

Figure 7 shows the entire known population of pulsars within 5° of the ecliptic. These pulsars come within $20 R_\odot$ or less of the Sun when in solar conjunction, some of them being fully eclipsed by the Sun. For comparison, NASA’s Parker Solar Probe will come within approximately $5 R_\odot$ of the Sun’s surface. A high-cadence, low-frequency pulsar observing campaign through approximately December and January, when the bulk of the near-ecliptic pulsar population drifts behind the

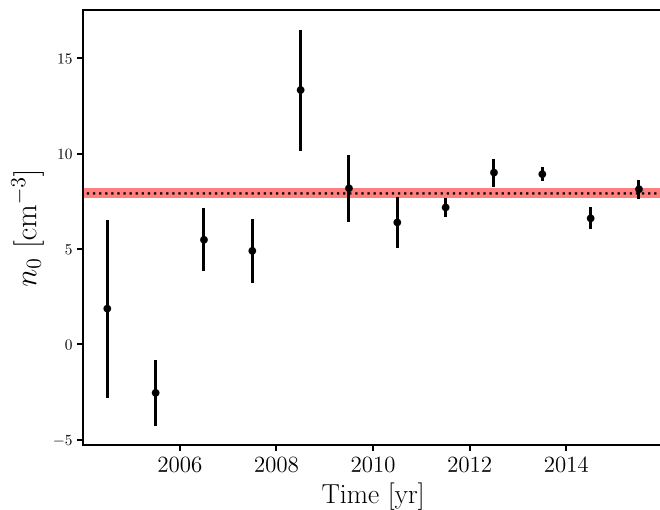


Figure 7. Best-fit values of the solar wind electron density at 1 au, n_0 , when it is allowed to vary from year to year. We show results for only the final 10 yr of the 11 yr data set because the best-fit values for n_0 from the first approximately 1.4 yr of data are within 2σ of zero, effectively a nondetection. The black dotted line shows the best-fit value of n_0 when we assume it is constant throughout our data set; the red shaded region indicates the 1σ uncertainties on that value.

Sun, paired with the analysis techniques we have developed here, could map out the large-scale structure of the SW and powerfully complement the in situ capabilities of the Parker Solar Probe. Telescopes like the Canadian Hydrogen Intensity Mapping Experiment (CHIME/FRB Collaboration et al. 2018), the Long Wavelength Array (Ellingson et al. 2009), the Murchison Widefield Array (Tingay et al. 2012), and LOFAR (van Haarlem et al. 2013) are well suited for this kind of high-cadence observational campaign.

Additionally, pulsars are strongly linearly polarized and are thus very useful for probing the Sun’s magnetic field (Bird et al. 1980; You et al. 2012). The type of many-pulsar analysis we have developed in this work could be straightforwardly extended to an analysis of rotation measures to make unprecedented inferences about the large-scale configuration of the Sun’s magnetic field. A high-cadence, low-frequency observing campaign would also be ideal for this application.

Author contributions: D.R.M. wrote this manuscript and developed the techniques it describes. J.M.C. made code for simulating screens of turbulent material in the interstellar medium. D.J.N. conducted a preliminary analysis of the annual component of dispersion measure variations. J.M.C., C.M.F. M., D.J.N., M.T.L., M.A.M., and S.C. reviewed and substantially improved this manuscript. Z.A., K.C., P.B.D., M.E.D., T.D., J.A.E., R.D.F., E.C.F., E.F., P.A.G., G.J., M.L.J., M.T.L., L.L., D.R.L., R.S.L., M.A.M., C.N., D.J.N., T.T.P., S.M.R., P.S.R., R.S., I.H.S., K.S., J.K.S., and W.W.Z. contributed to the development of the 11 yr data set, as detailed in Arzoumanian et al. (2018a).

The NANOGrav project receives support from National Science Foundation (NSF) Physics Frontiers Center award No. 1430284. D.R.M. is a Jansky Fellow of the National Radio Astronomy Observatory (NRAO). NRAO is a facility of the NSF operated under cooperative agreement by Associated Universities, Inc. The Arecibo Observatory is operated by SRI International under cooperative agreement with the NSF (AST-1100968), and

in alliance with Ana G. Méndez-Universidad Metropolitana and the Universities Space Research Association. The Green Bank Observatory is a facility of the NSF operated under a cooperative agreement by Associated Universities, Inc. The Flatiron Institute is supported by the Simons Foundation. Pulsar research at UBC is supported by an NSERC Discovery Grant and by the Canadian Institute for Advanced Research.

ORCID iDs

D. R. Madison <https://orcid.org/0000-0003-2285-0404>
 J. M. Cordes <https://orcid.org/0000-0002-4049-1882>
 S. Chatterjee <https://orcid.org/0000-0002-2878-1502>
 M. E. DeCesar <https://orcid.org/0000-0002-2185-1790>
 T. Dolch <https://orcid.org/0000-0001-8885-6388>
 M. T. Lam <https://orcid.org/0000-0003-0721-651X>
 L. Levin <https://orcid.org/0000-0002-2034-2986>
 R. S. Lynch <https://orcid.org/0000-0001-5229-7430>
 M. A. McLaughlin <https://orcid.org/0000-0001-7697-7422>
 D. J. Nice <https://orcid.org/0000-0002-6709-2566>
 T. T. Pennucci <https://orcid.org/0000-0001-5465-2889>
 S. M. Ransom <https://orcid.org/0000-0001-5799-9714>
 P. S. Ray <https://orcid.org/0000-0002-5297-5278>
 R. Spiewak <https://orcid.org/0000-0002-6730-3298>
 I. H. Stairs <https://orcid.org/0000-0001-9784-8670>
 K. Stovall <https://orcid.org/0000-0002-7261-594X>
 J. K. Swiggum <https://orcid.org/0000-0002-1075-3837>

References

- Archibald, A. M., Gusinskaia, N. V., Hessels, J. W. T., et al. 2018, *Natur*, 559, 73
 Armstrong, J. W., Rickett, B. J., & Spangler, S. R. 1995, *ApJ*, 443, 209
 Arzoumanian, Z., Baker, P. T., Brazier, A., et al. 2018b, *ApJ*, 859, 47
 Arzoumanian, Z., Brazier, A., Burke-Spolaor, S., et al. 2018a, *ApJS*, 235, 37
 Bird, M. K., Schreifer, E., Volland, H., & Sieber, W. 1980, *Natur*, 283, 459
 Caballero, R. N., Lee, K. J., Lentati, L., et al. 2016, *MNRAS*, 457, 4421
 CHIME/FRB Collaboration, Amiri, M., Bandura, K., et al. 2018, *ApJ*, 863, 48
 Coles, W. A., Kerr, M., Shannon, R. M., et al. 2015, *ApJ*, 808, 113
 Cordes, J. M., Shannon, R. M., & Stinebring, D. R. 2016, *ApJ*, 817, 16
 Counselman, C. C., III, & Rankin, J. M. 1972, *ApJ*, 175, 843
 Counselman, C. C., III, & Shapiro, I. I. 1968, *Sci*, 162, 352
 Desvignes, G., Caballero, R. N., Lentati, L., et al. 2016, *MNRAS*, 458, 3341
 DuPlain, R., Ransom, S., Demorest, P., et al. 2008, *Proc. SPIE*, 7019, 70191D
 Edwards, R. T., Hobbs, G. B., & Manchester, R. N. 2006, *MNRAS*, 372, 1549
 Ellingson, S. W., Clarke, T. E., Cohen, A., et al. 2009, *IEEEP*, 97, 1421
 Goldstein, S. J., & Meisel, D. D. 1969, *Natur*, 224, 349
 Hobbs, G. 2013, *CQGrA*, 30, 224007
 Hollweg, J. V. 1968, *Natur*, 220, 771
 Howard, T. A., Stovall, K., Dowell, J., Taylor, G. B., & White, S. M. 2016, *ApJ*, 831, 208
 Issautier, K., Le Chat, G., Meyer-Vernet, N., et al. 2008, *GeoRL*, 35, L19101
 Issautier, K., Meyer-Vernet, N., Moncuquet, M., & Hoang, S. 1997, *SoPh*, 172, 335
 Issautier, K., Meyer-Vernet, N., Moncuquet, M., & Hoang, S. 1998, *JGR*, 103, 1969
 Issautier, K., Moncuquet, M., & Hoang, S. 2004, *SoPh*, 221, 351
 Jones, M. L., McLaughlin, M. A., Lam, M. T., et al. 2017, *ApJ*, 841, 125
 Keith, M. J., Coles, W., Shannon, R. M., et al. 2013, *MNRAS*, 429, 2161
 Kramer, M., & Champion, D. J. 2013, *CQGrA*, 30, 224009
 Lam, M. T., Cordes, J. M., Chatterjee, S., et al. 2016, *ApJ*, 819, 155
 Lam, M. T., Cordes, J. M., Chatterjee, S., et al. 2017, *ApJ*, 834, 35
 Lam, M. T., Cordes, J. M., Chatterjee, S., & Dolch, T. 2015, *ApJ*, 801, 130
 Lam, M. T., Ellis, J. A., Grillo, G., et al. 2018b, *ApJ*, 861, 132
 Lam, M. T., McLaughlin, M. A., Cordes, J. M., Chatterjee, S., & Lazio, T. J. W. 2018a, *ApJ*, 861, 12
 Leblanc, Y., Dulk, G. A., & Bougeret, J.-L. 1998, *SoPh*, 183, 165
 Levin, L., McLaughlin, M. A., Jones, G., et al. 2016, *ApJ*, 818, 166
 Lommen, A. N., Kipporn, R. A., Nice, D. J., et al. 2006, *ApJ*, 642, 1012
 Manchester, R. N., Hobbs, G. B., Teoh, A., & Hobbs, M. 2005, *AJ*, 129, 1993
 Matthews, A. M., Nice, D. J., Fonseca, E., et al. 2016, *ApJ*, 818, 92
 Nice, D., Demorest, P., Stairs, I., et al. 2015, Tempo: Pulsar Timing data Analysis, Astrophysics Source Code Library, ascl:1509.002

- Niu, Z.-X., Hobbs, G., Wang, J.-B., & Dai, S. 2017, *RAA*, **17**, 103
- Parker, E. N. 1958, *ApJ*, **128**, 664
- Ransom, S. M., Demorest, P., Ford, J., et al. 2009, AAS Meeting 214, 605.08
- Reardon, D. J., Hobbs, G., Coles, W., et al. 2016, *MNRAS*, **455**, 1751
- Rickett, B. J. 1990, *ARA&A*, **28**, 561
- Schwenn, R. 2006, *LRSP*, **3**, 2
- Splaver, E. M., Nice, D. J., Stairs, I. H., Lommen, A. N., & Backer, D. C. 2005, *ApJ*, **620**, 405
- The Astropy Collaboration, Price-Whelan, A. M., Sipőcz, B. M., et al. 2018, *AJ*, **156**, 123
- The NANOGrav Collaboration, Arzoumanian, Z., Brazier, A., et al. 2015, *ApJ*, **813**, 65
- Tiburzi, C., & Verbiest, J. 2018, in Proc. IAU Symp. 337, Pulsar Astrophysics the Next Fifty Years (Cambridge: Cambridge Univ. Press), 279
- Tingay, S., Goeke, R., Hewitt, J. N., et al. 2012, *PoS*, **163**, 36
- van Haarlem, M. P., Wise, M. W., Gunst, A. W., et al. 2013, *A&A*, **556**, A2
- van Haasteren, R., & Levin, Y. 2013, *MNRAS*, **428**, 1147
- VanderPlas, J. T., & Ivezić, Ž. 2015, *ApJ*, **812**, 18
- Vigeland, S. J., & Vallisneri, M. 2014, *MNRAS*, **440**, 1446
- Wang, P. F., & Han, J. L. 2018, *MNRAS*, **479**, 3393
- You, X. P., Coles, W. A., Hobbs, G. B., & Manchester, R. N. 2012, *MNRAS*, **422**, 1160
- You, X. P., Hobbs, G. B., Coles, W. A., Manchester, R. N., & Han, J. L. 2007, *ApJ*, **671**, 907